

Quantifying Photocurrent Loss of a Single Particle–Particle Interface in Nanostructured Photoelectrodes

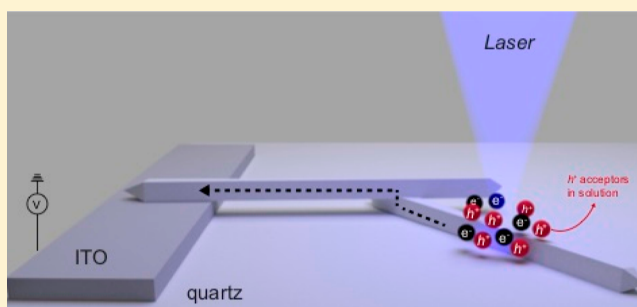
Mahdi Hesari,¹ Justin B. Sambur,¹ Xianwen Mao, Won Jung, and Peng Chen*

Department of Chemistry and Chemical Biology, Cornell University, Ithaca, New York 14853, United States

Supporting Information

ABSTRACT: Particle–particle interfaces are ubiquitous in nanostructured photoelectrodes and photovoltaics, which are important devices for solar energy conversion. These interfaces are expected to cause performance losses in these devices, but how much loss they would incur is poorly defined. Here we use a subparticle photoelectrochemical current measurement, in combination with specific photoelectrode configurations, to quantify the current losses from single particle–particle interfaces formed between individual TiO₂ nanorods operating as photoanodes in aqueous electrolytes. We find that a single interface leads to ~20% photocurrent loss (i.e., ~80% retention of the original current). Such quantitative, first-of-its-kind, information provides a metric for guiding the optimization and design of nanostructured photoelectrodes and photovoltaics.

KEYWORDS: *Subparticle photoelectrochemistry, interface losses, single nanorod photoelectrodes*



Increase in energy demand in our daily life, limits in conventional energy resources, and generation of greenhouse gases have motivated much research in harvesting solar energy.¹ Photoelectrodes and photovoltaics, both made of semiconductor materials, are crucial devices that can harvest light energy to convert to chemical energy and/or electricity.^{2,3} Nanostructured photoelectrodes and photovoltaics, for example, thin films of semiconductor nanoparticles,⁴ often offer enhanced overall performance^{5–8} resulting from their large surface-to-volume ratios,⁹ tunable bandgaps through quantum confinement,^{10–13} and possibly different combinations of exposed surface facets,^{14–16} which could impact their light absorption as well as the separation, transport, and recombination properties of charge carriers.

A ubiquitous feature of nanostructured photoelectrodes or photovoltaics is the presence of particle–particle interfaces. The electrical current has to pass through these interfaces, which are less conductive, leading to current loss and decreased device performance. Quantifying the current loss through these interfaces is thus crucial for providing a fundamental metric to guide material design and device optimization to minimize loss. This quantification is challenging experimentally, however, because a nanostructured film contains a large number of nanoparticles and a heterogeneous collection of interfaces. Moreover, many electrical paths are possible; each of them may go through a different number of interfaces to reach the back contact electrode.¹⁷ All of these make bulk electrical current measurements incapable of dissecting the contributions of individual interfaces.

Here, we report subparticle photoelectrochemical current measurements to quantify the losses from single particle–particle interfaces between single TiO₂ nanorods. Our measurements utilize specific cross geometries between two nanorods as well as site-selective measurements, in which the photoelectrochemical current passes zero or merely one interface; the latter was found to give rise to ~20% photocurrent loss under photoanodic operating conditions in aqueous electrolytes.

We used a microfluidic photoelectrochemical cell with a three-electrode configuration to perform photoelectrochemical current measurements on an inverted optical microscope (Figure 1A). The working electrode is a transparent patterned indium tin oxide (ITO) electrode, which comprises many long, 100 nm-thick ITO strips, each ~11 μm in width separated by ~4 μm on a quartz substrate (Figure S2). We chose rutile TiO₂ nanorods¹⁸ of 181 ± 7 nm in diameter and a few microns in length as the photoanode material (Figure S1), as they are stable as photoanodes for water oxidation,^{19–21} and we have previously characterized their photoelectrochemistry at the subparticle level.^{22,23} We spin-casted these nanorods on the ITO electrode at low density and further annealed them at 450 °C for 1 h to improve the contact with the ITO strips (and, when applicable, nanorod–nanorod contacts). Sometimes two nanorods form a cross structure (i.e., possessing a single particle–particle interface) and are located on the quartz part of the electrode with one arm in contact with the ITO strip

Received: October 17, 2018

Revised: December 21, 2018

Published: January 7, 2019

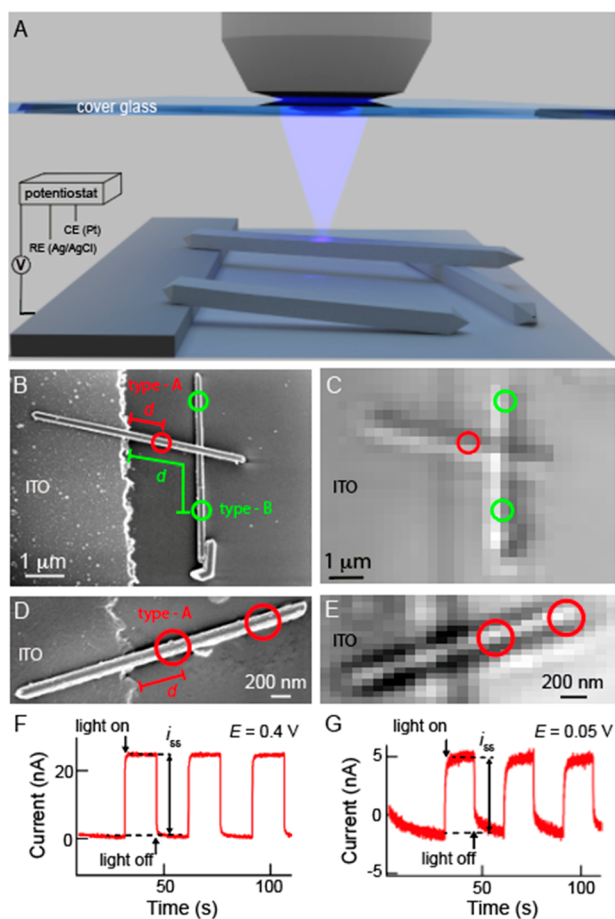


Figure 1. Subnanorod single-spot measurements of photoelectrochemical currents. (A) Illustration of subnanorod photoelectrochemical current measurements via focused laser excitation of individual TiO_2 nanorods dispersed on a patterned ITO working electrode in a three-electrode microfluidic photoelectrochemical cell. (B, C) SEM (B) and optical transmission image (C) of two nanorods forming a cross structure, with one arm in contact with the ITO strip. The circles denote the size and location of the 375 nm laser focus positioned either before (type-A, red) or after (type-B, green) the particle–particle interface. (D, E) Same as (B, C) but for a single nanorod. (F, G) Representative current vs time traces at +0.4 V (F) and +0.05 V (G) vs Ag/AgCl during three light-on (15 s) and light-off (15 s) periods in the presence of 0.6 M SO_3^{2-} in a pH 8.3, 0.1 M borate, and 1 M Na_2SO_4 aqueous solution. Data measured at the type-A spot in (B, C).

(Figure 1B,C). More often an isolated nanorod sits across an ITO–quartz edge (Figure 1D,E). Both configurations are readily identifiable under scanning electron microscopy and optical transmission microscopy (Figure 1B–E).

We focused a 375 nm laser (focus diameter ~ 380 nm; Figure S4) to locally generate charge carriers at a single spot on a cross structure and measured the corresponding photoelectrochemical current through the ITO electrode in aqueous electrolyte solutions (Figure 1A). This photocurrent reflects the local behaviors of the photogenerated charge carriers because of the charge carriers' small diffusion length (~ 100 nm) in TiO_2 ,²⁴ as we showed previously,²² and because there are no significant waveguiding effects by these nanorods under our experimental conditions (e.g., the nanorods absorb strongly the 375 nm light, and their diameters are much smaller than the excitation light wavelength; SI Section 3.1).

The laser focus can be positioned at a spot before the particle–particle interface (i.e., type-A spots) or after (i.e., type-B spots), relative to the electrical contact with ITO (Figure 1B). For the latter, the photocurrent has to go through the single particle–particle interface to reach the ITO electrode.

In a N_2 -purged, slightly basic aqueous electrolyte solution (i.e., 0.1 M pH 8.3 sodium borate buffer with 1 M Na_2SO_4), the photoanodic current generated on such TiO_2 nanorods is known to be dominated by water oxidation up to the potential of ~ 1.2 V (all potentials in this study are referenced to the Ag/AgCl electrode).²² But the efficiency is low because of the low efficiency of TiO_2 surfaces in catalyzing the water oxidation reaction. To increase the measurable photoanodic current, we added a hole scavenger SO_3^{2-} in the electrolyte (i.e., 0.6 M Na_2SO_3), which is known to enhance the overall photoanodic current (Figure S9).^{25–28} The hole scavenger also renders the semiconductor-to-electrolyte interfacial charge-transfer faster and thus less rate-limiting in generating the overall photoanodic current, making it more likely to observe the effect of a particle–particle interface in the photocurrent.

We first examined subnanorod measurements at spots where the photocurrent does not go through a particle–particle interface (i.e., type-A spots; the red circles in Figure 1B–E). At a sufficiently positive potential (e.g., +0.4 V), when the 375 nm laser is turned on or off every 15 s, the electrochemical current from a single nanorod spot follows a square-wave behavior with a clear anodic (i.e., positive) photocurrent that reaches steady state promptly (Figure 1F). At a less positive potential (e.g., +0.05 V), the current is less square-wave like, and the magnitude of the photocurrent is expectedly smaller (Figure 1G). In this study we focus on the steady-state photocurrent (i_{ss} , Figure 1F,G), in which the background contribution from the patterned ITO electrode was also subtracted out (SI Section 2.4).

At the positive potential of +0.4 V and when averaged over ~ 150 nanorod spots, the average single-spot photocurrent $\langle i_{ss} \rangle$ scales linearly with the power density of the 375 nm laser in the range of ~ 0.005 to 0.11 MW cm^{-2} (Figure 2A, open red circles). The same linear scaling is observed for the bulk steady-state photocurrent i_{bulk} measured over many TiO_2 nanorods on an ITO working electrode in the range from ~ 0.16 to 4.35 mW cm^{-2} (Figure 2A, open blue squares). This

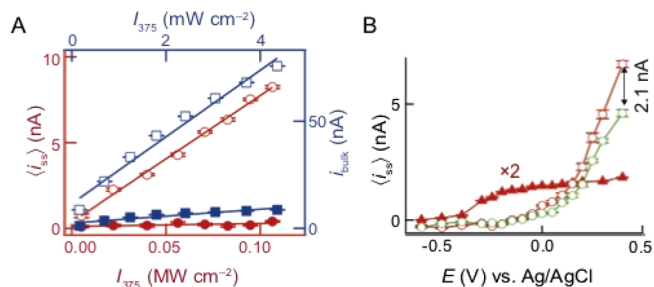


Figure 2. Averaged single-spot and bulk photocurrent dependences on light power density and potential. (A) Averaged single-spot steady-state photocurrent $\langle i_{ss} \rangle$ (red symbols; 150 spots averaged) and bulk steady-state photocurrent i_{bulk} (blue symbols) vs I_{375} , the 375 nm laser power density, in the presence (open symbols) and absence of (solid symbols) of the hole scavenger at +0.4 V. (B) Averaged single-spot steady-state photocurrent vs potential (averaged over ~ 150 spots) in the presence (open symbols) or absence (solid triangles) of the hole scavenger SO_3^{2-} and at type-A (red) or type-B (green) spots. $I_{375} = 0.056$ MW cm^{-2} .

linear dependence of the steady-state photocurrent on the light power density was also observed when TiO₂ nanorods were lying entirely on an ITO electrode, as we showed previously.²² In the absence of the hole scavenger SO₃²⁻, the steady-state photocurrents show the same linear dependences on the light power density, but the magnitudes are ~ 10 times smaller, as expected (Figure 2A, solid symbols). Because of these linear dependences, we chose the relatively large power density of ~ 0.06 MW cm⁻² for all subsequent single-spot measurements so that the photocurrents could still be reliably measured even at much less positive potentials. It is worth noting that under this single-spot illumination condition, the light-induced heating is still insignificant, as heat conduction calculations show that the temperature at the center of the illumination spot on the nanorod is < 1 K higher than room temperature (SI Section 3.2).

We next examined how the single-spot photocurrent depends on the applied potential at type-A spots. In the absence of the hole scavenger and at a fixed light power density, the steady-state photocurrent $\langle i_{ss} \rangle$ averaged over many individual spots shows a clear potential dependence: It onsets at about -0.4 V and increases toward more positive potentials (Figure 2B, solid red triangles), analogous to what was observed previously on TiO₂ nanorods that were in full contact with an ITO electrode.²² In the presence of the hole scavenger, the onset potential of $\langle i_{ss} \rangle$ shifts positively to ~ 0.1 V, in agreement with ensemble photocurrent behaviors (Figure S11C and SI Section 3.4). More importantly and expectedly, its magnitude at positive potentials (e.g., $+0.4$ V) increases to ~ 7 nA, a factor of ~ 7 larger than that in the absence of the hole scavenger (Figure 2B, open red circles vs solid red triangles).

We then moved onto examining the behaviors at the type-B spots where the current has to go through a single particle–particle interface and performed measurements on a total of 59 cross structures of TiO₂ nanorods. Strikingly, in the presence of the hole scavenger, $\langle i_{ss} \rangle$ decreased significantly compared with that at the type-A spots, although the onset potential stays essentially unchanged (Figure 2B, open green vs open red symbols). At the positive potential of $+0.4$ V, the decrease is ~ 2.1 nA, corresponding to $\sim 31\%$ decrease from that of the type-A spots and clearly reporting the photocurrent loss stemming from a single particle–particle interface in the cross structures of nanorods. It is worth noting that to determine the contribution of the particle–particle interface, measurement right at the cross is undesirable because in such a measurement, both the top and the bottom nanorods would be excited simultaneously.

Although the averaged single-spot behaviors of type-A vs type-B spots in Figure 2B strongly suggest a photocurrent loss due to a single particle–particle interface, there is a complication from their differences in distance (d) to the electrode edge (Figure 1B). Every spot we measured differs somewhat in its d , and on average, the type-B spots, which are located after the cross, are further away from the ITO electrode edge than the type-A spots. As the electrochemical potential is applied on the ITO strip electrode and TiO₂ nanorods are semiconductors, a drop in potential is expected along the nanorod length away from the ITO electrode edge. Consequently, the distance difference between type-A and type-B spots will result in their different actual local potentials, which could contribute to the difference in their measured photocurrents.

To decouple this effect of distance from the electrode edge, we examined how the measured i_{ss} of each spot depends on its distance to the electrode edge, d , in the presence of the hole scavenger at fixed applied potentials. We focused on the more positive potential range here (i.e., $+0.2$ to $+0.4$ V), where the photoanodic currents are significant. For the type-A spots, their individual i_{ss} vs d shows a lot of scatter (e.g., at $+0.4$ V; red points, Figure 3A; and Figure S13 at $+0.3$ and $+0.2$ V); this

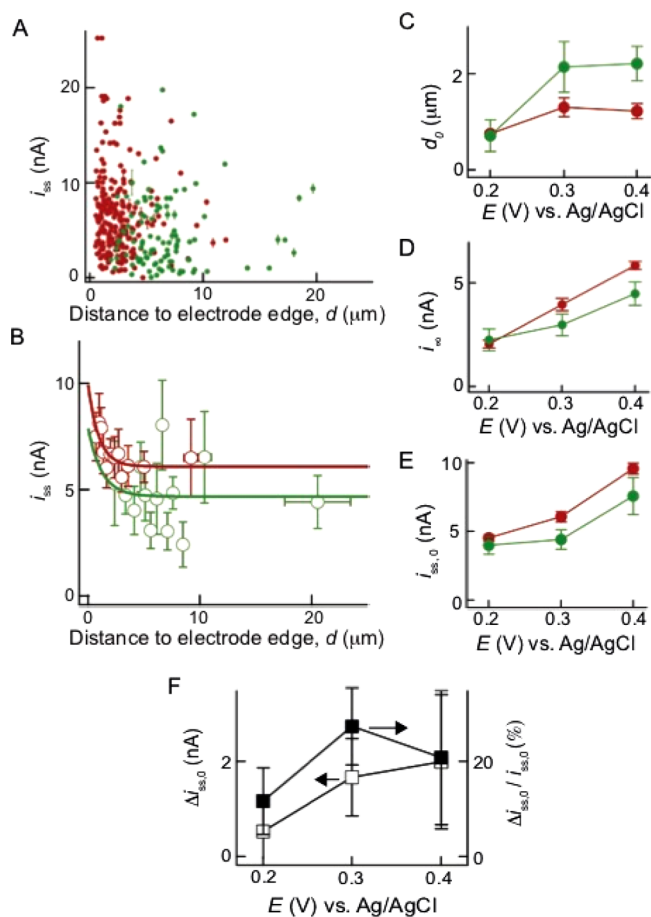


Figure 3. Photocurrent loss from a single particle–particle interface between TiO₂ nanorods. (A) Steady-state photocurrent i_{ss} at individual nanorod spots vs their distances to electrode edge d in the presence of hole scavenger at $+0.4$ V. Each point is from one spot. Red points: type-A spots; green points: type-B spots. Total 59 cross structures of nanorods were measured. (B) Data points from A are binned every 12 points and averaged to get general trends (symbols); x , y error bars are s.d. and s.e.m., respectively. Lines are fits with eq 1. (C–E) Potential dependences of fitted d_0 , i_∞ , and $i_{ss,0}$ from B for type-A (red) and type-B (green) spots. (F) Absolute (open squares, left axis) and relative (in percentage, solid squares, right axis) photocurrent losses due to a single particle–particle interface calculated from (E).

scatter is not surprising because these nanorods have large intra- and internanorod heterogeneity at the subparticle level, as we showed previously,²² which likely stems from the inhomogeneous distribution of structural defects and impurity metal atoms on their surfaces. Moreover, position variation of the laser focus spot perpendicular to the nanorod long axis could also contribute to this scatter of data points. However, upon binning and averaging within each bin of similar d , the i_{ss} shows a clear decreasing trend with increasing distance from

the electrode edge (Figure 3B, red points); it follows an approximate exponential decay:

$$i_{ss} = i_0 \times \exp(-d/d_0) + i_\infty \quad (1)$$

Here the exponential decay function was chosen to empirically model the behavior of experimental data, while also fulfilling a few limiting physical constraints with a minimal number of parameters: (i) at $d = 0$, the photocurrent should have a finite value; (ii) with increasing d , the photocurrent should decay gradually; and (iii) when d becomes very large, the photocurrent should approach a limiting value. Moreover, the exponential decay function contains a characteristic distance scale represented by the decay distance constant d_0 .

Fitting the data with eq 1 gives an exponential decay distance d_0 here of $\sim 0.9 \mu\text{m}$ at the applied potential of 0.2 V (Figure 3C), and d_0 slightly increases with more positive potentials (Figure 3C, red points). This decay distance likely reflects a characteristic distance of potential drop along the length of the nanorod; it could also have contributions from current losses while traveling through the nanorod (e.g., from charge carrier scattering by impurities atoms). The residual photocurrent i_∞ is $\sim 2 \text{ nA}$ at 0.2 V (Figure 3D), reflecting a limiting steady-state photocurrent at long distances away from the electrode edge under our experimental conditions; a nonzero residual photocurrent i_∞ here is not surprising, as the nanorod still has a certain potential relative to that of the electrolyte solution even when the distance is large. Expectedly, i_∞ is larger at more positive potentials (Figure 3D, red points). More important, we could extrapolate i_{ss} to $d = 0$ (i.e., $i_{ss,0}$); this value represents the single-spot steady-state photocurrent when the measured spot is right at the electrode edge ($\sim 4.5 \text{ nA}$ at +0.2 V) and is larger at more positive potentials expectedly (Figure 3E, red points).

For the type-B spots where the photocurrent has to go through a single particle–particle interface, the individual spots show the similar heterogeneity (Figure 3A, green points). Upon binning and averaging, i_{ss} follows the similar exponential decay with increasing d (Figure 3B, green points). However, the decay distance d_0 is longer (Figure 3C) compared with that of type-A spots, likely reflecting the contribution of the interface. The residual photocurrent i_∞ at long distances is smaller in general (Figure 3D), and most importantly, the extrapolated $i_{ss,0}$ at $d = 0$ is also smaller (Figure 3E), both reflecting a photocurrent loss due to the presence of a single particle–particle interface.

We calculated $\Delta i_{ss,0}$, the average photocurrent loss due to a single particle–particle interface directly at the electrode (the photocurrent losses from individual cross structures are presented in Figure S14). The $\Delta i_{ss,0}$ varies from about 0.5 to 2 nA in the potential range from +0.2 to +0.4 V under our experimental conditions (Figure 3F, open squares), representing about 11–27% photocurrent loss relatively (averaging $\sim 20\%$; Figure 3G, solid squares). In other words, after passing through one particle–particle interface, only $\sim 80\%$ photocurrent remains. By extrapolation, passage through ~ 11 interfaces would lead to the photocurrent to drop below $\sim 10\%$ of the original (i.e., $(80\%)^{11} \approx 9\%$).

Although the nature of the interfaces between the nanorods here is unclear (e.g., there could be a miniature amount of water), these interfaces were formed using procedures similar to those in making bulk film photoelectrodes of TiO_2 nanoparticles, including the absence of surfactants on the nanorods, spin-casting for deposition on the electrode, and

subsequent thermal annealing to improve contacts. Therefore, these interfaces should be similar and thus relevant to those interfaces in bulk nanoparticle film photoelectrodes.

In summary, we have used a subparticle photoelectrochemistry microscopy approach to measure the photocurrent losses from single particle–particle interfaces in TiO_2 -nanorod-based photoanodes. This loss amounts to $\sim 20\%$ of the photocurrent, quantifying the significant performance loss from a single interface. Moreover, this $\sim 20\%$ loss is largely independent of the applied electrochemical potential in the range from +0.2 to +0.4 V (Figure 3F); this independence suggests that the loss mechanism is likely not due to factors that depend on the applied potential, such as the depletion region width or the potential drop across the interface. Overall, such a metric for photocurrent loss should be a useful quantitative reference for optimizing and designing nanostructured photoelectrodes (or photovoltaics) where interfaces are prevalent.

■ ASSOCIATED CONTENT

📄 Supporting Information

The Supporting Information is available free of charge on the ACS Publications website at DOI: 10.1021/acs.nanolett.8b04188.

Details of TiO_2 nanorod characterization, IDA-ITO electrode dimension, 375 nm laser focus size determination, electrochemical flow cell assembly, photocurrent vs time trace analysis, determination of distance of photocurrent measurement positions to the electrode edge, and calculation of the spatial temperature profile under laser illumination (PDF)

■ AUTHOR INFORMATION

Corresponding Author

*E-mail: pc252@cornell.edu.

ORCID

Mahdi Hesari: 0000-0002-5598-3468

Justin B. Sambur: 0000-0002-8457-4946

Present Address

†Colorado State University, Department of Chemistry, Fort Collins, CO, 80528, United States.

Notes

The authors declare no competing financial interest.

■ ACKNOWLEDGMENTS

This research is primarily supported by the Department of Energy, Office of Science, Basic Energy Sciences, Catalysis Science Program, under award DE-SC0004911. Efforts by X. Mao were in part supported by U.S. Army Research Office under grant nos. W911NF-17-1-0590 and W911NF-18-1-0217. This work made use of the Cornell Center for Materials Research Shared Facilities, which are supported through the NSF MRSEC program (grant no. DMR-1719875). We also thank Malcolm Thomas for his help on SEM imaging at CCMR.

■ REFERENCES

- (1) Chu, S.; Cui, Y.; Liu, N. *Nat. Mater.* **2017**, *16*, 16.
- (2) Sivula, K.; van de Krol, R. *Nat. Rev. Mater.* **2016**, *1*, 15010.
- (3) Aruchamy, A. *Photoelectrochemistry and Photovoltaics of Layered Semiconductors*; Springer: Amsterdam, Netherlands, 2013.
- (4) Lee, T. D.; Ebong, A. U. *Renewable Sustainable Energy Rev.* **2017**, *70*, 1286.

- (5) Nozik, A. *Nano Lett.* **2010**, *10*, 2735.
- (6) Chen, H. M.; Chen, C. K.; Liu, R.-S.; Zhang, L.; Zhang, J.; Wilkinson, D. P. *Chem. Soc. Rev.* **2012**, *41*, 5654.
- (7) Hu, X.; Li, G.; Yu, J. C. *Langmuir* **2010**, *26*, 3031.
- (8) Yang, P.; Yan, R.; Fardy, M. *Nano Lett.* **2010**, *10*, 1529.
- (9) Grätzel, M. *Inorg. Chem.* **2005**, *44*, 6841.
- (10) Smith, A. M.; Nie, S. *Acc. Chem. Res.* **2010**, *43*, 190.
- (11) Brus, L. E. *J. Chem. Phys.* **1984**, *80*, 4403.
- (12) Kammler, D. R.; Mason, T. O.; Young, D. L.; Coutts, T. J.; Ko, D.; Poepelmeier, K. R.; Williamson, D. L. *J. Appl. Phys.* **2001**, *90*, 5979.
- (13) Ning, C.-Z.; Dou, L.; Yang, P. *Nat. Rev. Mater.* **2017**, *2*, 17070.
- (14) Choi, K.-S. *J. Phys. Chem. Lett.* **2010**, *1*, 2244.
- (15) Wang, W.; Zhou, Y.; Wen, Y.; Ni, Y.; Lu, C.; Xu, Z. *Mater. Lett.* **2015**, *158*, 29.
- (16) Tilley, S. D.; Cornuz, M.; Sivula, K.; Grätzel, M. *Angew. Chem., Int. Ed.* **2010**, *49*, 6405.
- (17) Yu, Y.; Protasenko, V.; Jena, D.; Xing, H.; Kuno, M. *Nano Lett.* **2008**, *8*, 1352.
- (18) Liu, B.; Chen, H. M.; Liu, C.; Andrews, S. C.; Hahn, C.; Yang, P. *J. Am. Chem. Soc.* **2013**, *135*, 9995.
- (19) Fujishima, A.; Zhang, X.; Tryk, D. A. *Surf. Sci. Rep.* **2008**, *63*, 515.
- (20) Wang, X.; Li, Z.; Shi, J.; Yu, Y. *Chem. Rev.* **2014**, *114*, 9346.
- (21) Berger, T.; Monllor-Satoca, D.; Jankulovska, M.; Lana-Villarreal, T.; Gómez, R. *ChemPhysChem* **2012**, *13*, 2824.
- (22) Sambur, J. B.; Chen, T.-Y.; Choudhary, E.; Chen, G.; Nissen, E. J.; Thomas, E. M.; Zou, N.; Chen, P. *Nature* **2016**, *530*, 77.
- (23) Sambur, J. B.; Chen, P. *J. Phys. Chem. C* **2016**, *120*, 20668.
- (24) Salvador, P. *J. Appl. Phys.* **1984**, *55*, 2977.
- (25) Berr, M. J.; Wagner, P.; Fischbach, S.; Vaneski, A.; Schneider, J.; Susha, A. S.; Rogach, A. L.; Jäckel, F.; Feldmann, J. *Appl. Phys. Lett.* **2012**, *100*, 223903.
- (26) Anthony Byrne, J.; Eggins, B. R.; Dunlop, P. S. M.; Linquette-Mailley, S. *Analyst* **1998**, *123*, 2007.
- (27) de Tacconi, N. R.; Mrkic, M.; Rajeshwar, K. *Langmuir* **2000**, *16*, 8426.
- (28) Kafizas, A.; Ma, Y.; Pastor, E.; Pendlebury, S. R.; Mesa, C.; Francàs, L.; Le Formal, F.; Noor, N.; Ling, M.; Sotelo-Vazquez, C.; Carmalt, C. J.; Parkin, I. P.; Durrant, J. R. *ACS Catal.* **2017**, *7*, 4896.